Chasing the multi-modal plasma response in MAST-U

OPEN ACCESS
IOP Publishing
Plasma Physics and Controlled Fusion
Plasma Phys. Control. Fusion **66** (2024) 065023 (15pp)
https://doi.org/10.1088/1361-6587/ad4419

Chasing the multi-modal plasma response in MAST-U

S Munaretto[1,*], Y Q Liu[2], D A Ryan[3], G Z Hao[4], J W Berkery[1], S Blackmore[3] and L Kogan[3]

[1] Princeton Plasma Physics Laboratory, 100 Stellarator Rd, Princeton, NJ 08540, United States of America
[2] General Atomics, PO Box 85608, San Diego, CA 92186, United States of America
[3] United Kingdom Atomic Energy Authority, Culham Campus, Abingdon OX14 3DB, United Kingdom
[4] Southwestern Institute of Physics, Chengdu, People's Republic of China

E-mail: smunaret@pppl.gov

Received 15 December 2023, revised 9 April 2024
Accepted for publication 26 April 2024
Published 8 May 2024

Abstract

Achieving edge localized modes (ELMs) suppression in spherical tokamaks by applying resonant magnetic perturbations (RMPs) has proven challenging. The poloidal spectrum of the applied RMP is a key parameter that has an impact on the capability to mitigate and eventually suppress ELMs. In this work the resistive magnetohydrodynamic code MARS-F (Liu *et al* 2000 *Phys. Plasmas* **7** 3681) is used to evaluate the possibility of directly measuring the plasma response in MAST-U, and particularly its variation as function of the applied poloidal spectrum, in order to guide the experimental validation of the predicted best RMP configuration for ELM suppression. Toroidal mode number $n = 2$ RMP is considered to minimize the presence of sidebands, and to avoid the deleterious core coupling of $n = 1$. Singular Value Decomposition is used to highlight linearly independent structures in the simulated magnetic 3D fields and how those structures can be measured at the wall where the magnetic sensors are located. Alternative ways to measure the multimodal plasma response and how they can be used to infer the best RMP configuration to achieve ELM suppression are also presented, including the plasma displacement and the 3D footprints at the divertor plates.

Keywords: MHD, plasma response, 3D fields, spherical tokamak, MAST-U

1. Introduction

A favorable plasma confinement regime in tokamaks is the so called 'high confinement regime', or 'H-mode' [1–3], where the formation of edge transport barriers allows for an increase of the global energy confinement time and an overall significant improvement of the plasma performances. However, the presence of steep edge profiles in a narrow layer inside the separatrix, often called the H-mode pedestal, leads to bursty plasma instabilities dubbed edge localized modes (ELMs) [4, 5]. ELMs are observed when either the pressure gradient or the edge current evolves to a state unstable to peeling and/or ballooning modes [6–8]. After the instability, the pressure gradient and the resulting current are relaxed. The pressure gradient then evolves back towards the pre-ELM state on the timescale of the confinement time, while the current gradient evolves on the longer current diffusion time. At some point the instability boundary is crossed again and the process repeats. Although the resulting impulsive heat load experienced by the plasma facing components at each ELM event does not pose a risk for the current experimental tokamaks, it is expected to damage the machine components of the International Thermonuclear Experimental Reactor and of future reactors [9–11]. For this reason the ELMs need to be completely suppressed or strongly mitigated.

* Author to whom any correspondence should be addressed.

ELM mitigation and control is a very active area of current fusion research [11]. The general approach to ELM control consists of providing additional energy transport through the pedestal to avoid reaching the ELM magnetohydrodynamic (MHD) stability limit and enough additional particle transport to make up for the suppressed ELM and avoid impurity accumulation in the plasma core [4]. Several means of ELM control exist, that are divided in three major categories: intrinsic ELM-free regimes, like the QH-mode [12]; ELM pacing, for example by vertical jogs [13], or by RMPs [14]; and ELM mitigation and suppression by RMPs [15–17]. The present work focuses on the latter.

While RMP ELM suppression is routinely achieved on a large number of conventional aspect ratio tokamaks, for example DIII-D [15], ASDEX-Upgrade [18], and KSTAR [19], it has proven challenging for spherical tokamaks (ST), where only ELM mitigation has been observed [20–23]. Among the several different factors that influence the capability of obtaining RMP ELM suppression, the choice of the poloidal spectrum of the applied perturbation plays a fundamental role by driving a different plasma response [21, 24, 25]. In this work the capability to directly measure the changes in plasma response on MAST-U [26] is explored using the linear resistive MHD code MARS-F [27], with the goal of providing a means to experimentally optimize the RMP poloidal spectrum independently while tuning other parameters like density and collisionality in order to achieve ELM suppression. The predictions presented in this manuscript will be validated against MAST-U experimental data once available.

The paper is organized as follows. In section 2 the MARS-F code is introduced, as well as the computational choices made for this work. In section 3 the results of the simulations are presented, with a particular focus on their dependence on the applied poloidal spectrum. Section 4 explores three different ways to directly measure the achievement of a favorable plasma response, followed by the conclusions in section 5.

2. Computational setup

2.1. The MARS-F model

While an extensive description of the linear resistive MHD code MARS-F can be found for example in [28], in this section a brief overview of what is relevant for the present work is presented. MARS-F solves the single-fluid, perturbed MHD equations in full toroidal geometry, expressed as follows:

$$i\left(\Omega_{\mathrm{RMP}}+n\Omega\right)\xi = \mathbf{v}+\left(\xi\cdot\nabla\Omega\right)R\hat{\phi} \tag{1}$$

$$\begin{aligned} i\rho\left(\Omega_{\mathrm{RMP}}+n\Omega\right)\mathbf{v} = &-\nabla p+\mathbf{j}\times\mathbf{B}+\mathbf{J}\times\mathbf{b}\\ &-\rho\left[2\Omega\hat{\mathbf{Z}}\times\mathbf{v}+\left(\mathbf{v}\cdot\nabla\Omega\right)R\hat{\phi}\right]\\ &+\nabla\cdot\left(\rho\xi\right)R^2\Omega^2\nabla\hat{Z}\times\nabla\phi\\ &-\rho\kappa_{\|}\left|k_{\|}v_{\mathrm{th},i}\right|\left[\mathbf{v}+\left(\xi\cdot\nabla\right)\mathbf{V}_0\right]_{\|} \end{aligned} \tag{2}$$

$$i\left(\Omega_{\mathrm{RMP}}+n\Omega\right)\mathbf{b} = \nabla\times\left(\mathbf{v}\times\mathbf{B}\right)+\left(\mathbf{b}\cdot\nabla\Omega\right)R\hat{\phi}-\nabla\times\left(\eta\mathbf{j}\right) \tag{3}$$

$$i\left(\Omega_{\mathrm{RMP}}+n\Omega\right)p = -\mathbf{v}\cdot\nabla P-\Gamma P\nabla\cdot\mathbf{v} \tag{4}$$

$$\mathbf{j} = \nabla\times\mathbf{b}. \tag{5}$$

R is the plasma major radius, $\hat{\phi}$ and $\hat{\mathbf{Z}}$ are the unit vectors along the geometric toroidal angle ϕ of the torus and the vertical direction in the poloidal plane respectively. Ω is the plasma toroidal rotation, Ω_{RMP} is the excitation frequency of the RMP field and n is the toroidal harmonic number. The plasma resistivity is denoted by η. The equilibrium magnetic field, current and pressure are denoted by $\mathbf{B}$, $\mathbf{J}$, P respectively, while $\mathbf{b}$, $\mathbf{j}$, p are their corresponding perturbed quantities. ρ is the plasma density, ξ is the plasma displacement, and $\mathbf{v}$ the perturbed plasma velocity. κ is a numerical coefficient determining the parallel sound wave damping 'strength' [29]. $k_{\|}=(n-m/q)/R$ is the parallel wave number, with m being the poloidal harmonic number and q being the safety factor. $v_{th,i}$ is the thermal ion velocity. The parallel component of the perturbed velocity is taken along the equilibrium field line. The damping term does not play a significant role at low-beta (as in the work presented here), but it is essential for high-beta plasmas [30, 31]. In this work it is fixed to $\kappa_{\|}=1.5$ for consistency with previous work on MAST [24].

For the RMP calculations, the vacuum field equations outside the plasma and the coil equations (Ampere's law) are solved together with the MHD equations for the plasma. The RMP field response modelling requires solving a linear antenna problem, where the source term is specified as the current flowing in the magnetic perturbation coils. Since this is a linear problem, for axisymmetric equilibria, only one single toroidal mode number n at one time is considered. The source current is assumed to have an $e^{in\phi}$ dependence along the toroidal angle ϕ. When looking for the steady-state response from the plasma, a flat-top DC coil current is applied, $\Omega_{\mathrm{RMP}}=0$.

In addition, the effect of magnetic field perturbations on the footprints on the outer divertor target surface is studied using the REORBIT module recently implemented in the MARS-F code [32–34]. The module traces the field lines—or the guiding-center drift orbit trajectories of test thermal particles—for a given field, including both 3D perturbation and 2D equilibrium field.

2.2. Equilibrium

The presented study is done starting from the experimental equilibrium from MAST-U shot 45 272 at $t=605$ ms, reconstructed using magnetic diagnostics [35] and Motional Stark Effect diagnostic [36] data. This equilibrium is characterized by a plasma current $I_{\mathrm{p}}=750$ kA, a toroidal magnetic field on axis $B_{\mathrm{T}}=0.59$ T, and a normalized ratio of the plasma pressure to the magnetic pressure $\beta_N=\beta_t aB_{\mathrm{T}}/I_{\mathrm{p}}\simeq 2$, where a is the plasma minor radius. A contour plot of the flux surfaces, along with the electron density, electron temperature, ion temperature, plasma toroidal frequency and safety factor (q) radial profiles, are shown in figures 1 and 2.

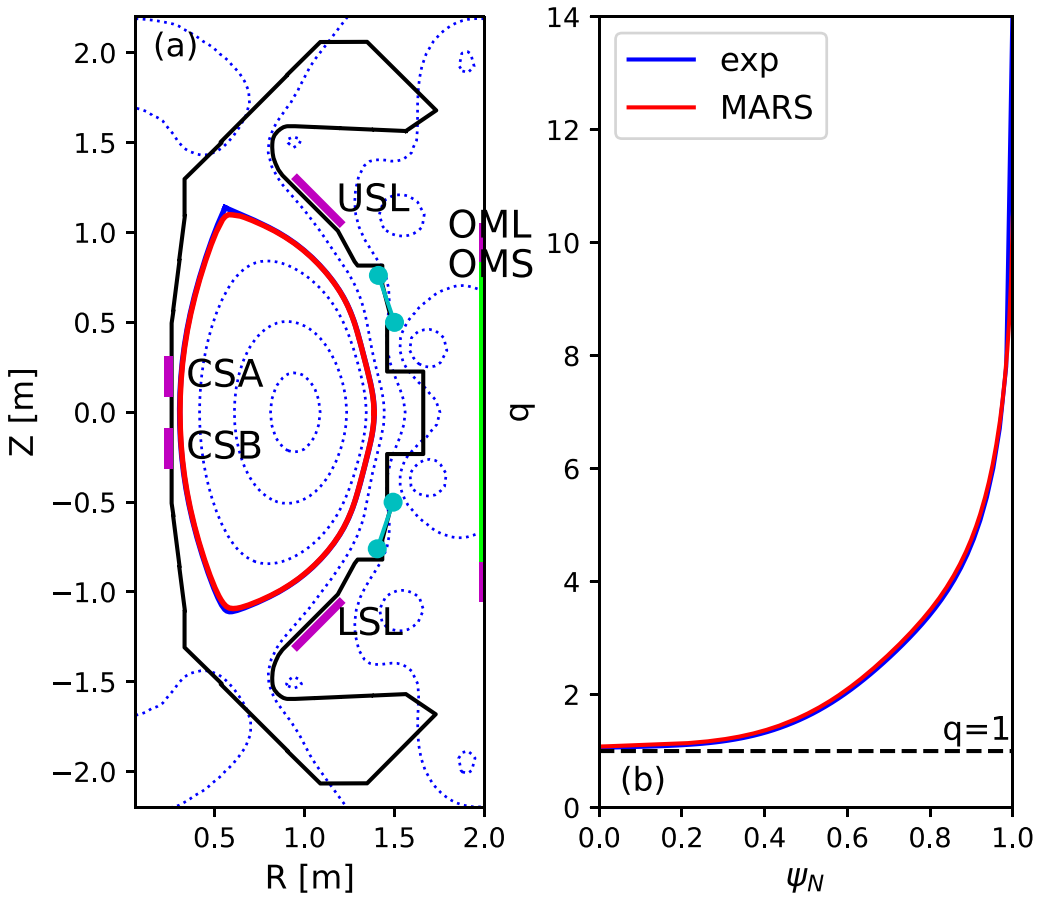

Figure 1. (a) Poloidal cross section of MAST-U. In black the limiter, in cyan the position of the RMP coils, in magenta and green the position of the arrays of saddle loops with their acronyms (CSA is the saddle loop array on the CenterStack Above the midplane, CSB that Below the midplane, USL and LSL the Upper and Lower Saddle Loop arrays respectively and OML and OMS the Outboard Midplane Large and Small saddle loop arrays respectively). The dotted blue lines are the experimental flux surfaces of the considered equilibrium, with the solid blue line showing the experimental last closed flux surface (LCFS). The solid red line is the LCFS used for the MARS-F simulations. In (b) there is the experimental safety factor (q) radial profile in blue and the modified q radial profile for the MARS-F simulations in red.

In divertor experiments, the q profile is not defined at the X-point, where there is zero poloidal field. In the MARS-F flux-based coordinate system, this would introduce a numerical singularity, and so a certain truncation scheme must be used to exclude the X point. Truncation effectively approximates the divertor configuration as a limiter configuration with an otherwise similar shape, imposing a finite q at the plasma edge, q_a. Although the truncation choice might have an impact on the plasma response calculation, it has been shown that the peeling response, the response that is of interest to obtain ELM suppression, is not affected by the X point truncation [37]. The truncated last closed flux surface (LCFS) and the resulting q radial profile are shown in red in figure 1, with $q_a^{\rm exp} \simeq 14.4$ and $q_a^{\rm MARS} \simeq 10.4$.

2.3. Toroidal perturbation

The set of coils used to produce the 3D perturbations in MAST-U and considered for this work are organized in two toroidal arrays located one above and one below the midplane. Their poloidal location is shown in cyan in figure 1(a). The coils are picture frame coils about 27 cm tall and they extend for about 20° in the toroidal direction. The upper row is comprised of 4 coils equally distributed, while the lower row has a total of 8 coils. The upper coils are vertically aligned with every other lower row coil. Each coil consists of four turns, such that $I_{\rm RMP} = 1$ kA corresponds to $I_{\rm RMP} = 4$ kAt.

Given the coils configuration, the applicable toroidal periodicity with the least amount of sidebands [38] is $n = 2$, and the chosen equilibrium is found to be stable for $n = 2$.

3. Plasma response to $n = 2$ perturbation

3.1. MARS-F results

To study the impact on the plasma response of different applied poloidal spectra, the relative phase between the applied field in the upper and the lower row of coils ($\Delta\phi = \phi_0^{\rm LOWER} - \phi_0^{\rm UPPER}$) is changed. As mentioned in section 2.1, the current in the coils is described as

$$I_{\rm COIL} = I_0 e^{{\rm i}(n\phi+\phi_0)}, \tag{6}$$

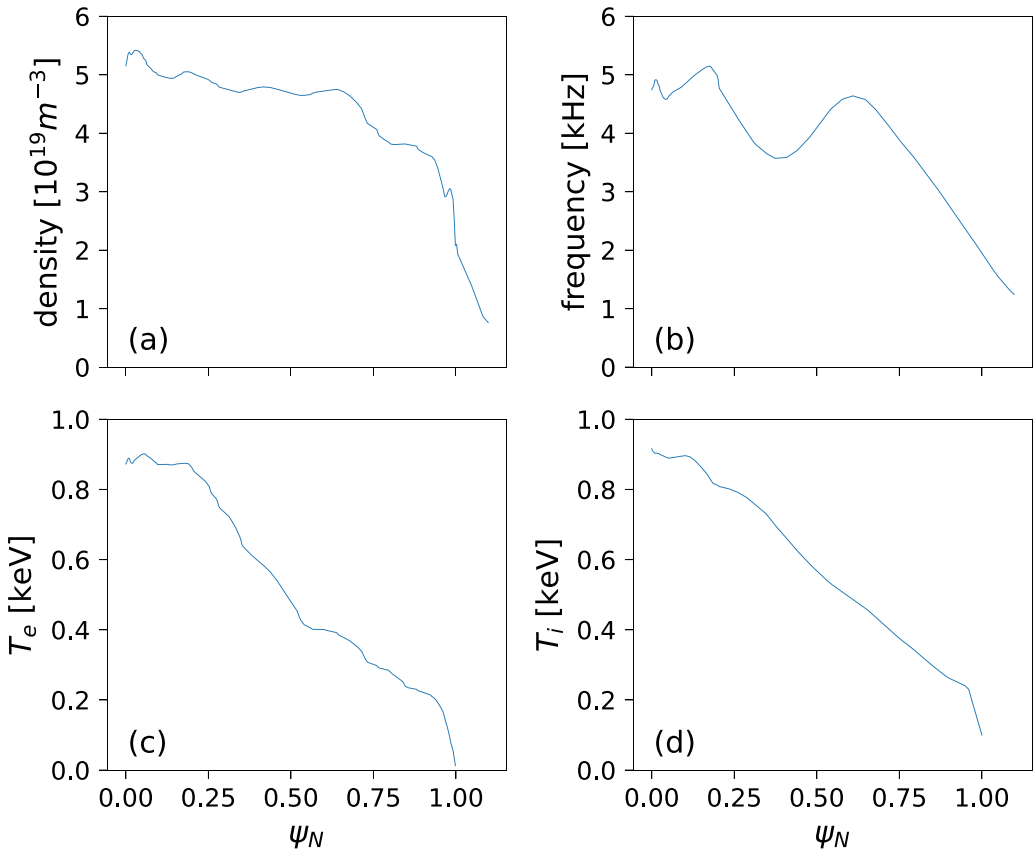

Figure 2. Experimental radial profiles used in the MARS-F simulations. (a) electron density, (b) toroidal frequency, (c) electron temperature, (d) ion temperature.

where I_0 is the amplitude of the applied perturbation and ϕ_0 the phase. To mimic what can be achieved in the MAST-U experiment, the changes in relative phase are obtained changing the phase of the lower row of coils while maintaining the upper row fixed. In this study the amplitude of the $n = 2$ perturbation produced by the upper and lower row of coils has been maintained equal. However, this does not translate to identical coil currents in the experiment due to the differing number of coils in each row. The amplitude of the magnetic field normal to the flux surfaces (δb_n) when the $n = 2$ perturbation is applied with different $\Delta\phi$ is shown in figure 3.

The impact of the plasma response as function of $\Delta\phi$ is more evident when the vacuum component of the field is removed. This is shown in figure 4 for the same four different applied perturbations. It can be noted that at $\Delta\phi = 90°$ the strongest plasma response is located in the upper and lower part of the plasma, while the field is negligible at the low field side (LFS) midplane. At $\Delta\phi = 270°$ the situation is the opposite, with most of the field concentrated in the LFS midplane. $\Delta\phi = 0°$ and $\Delta\phi = 180°$ are a combination of the two extreme cases. Also the response in the high field side (HFS) is different, with a larger response for $\Delta\phi = 90°$ and $\Delta\phi = 180°$ than for the other two cases.

Figure 5 shows the changes in the amplitude of the magnetic field tangential to the flux surfaces (δb_t). Similarly to the δb_n case, the amplitude at the top and bottom has a different dependence on $\Delta\phi$ than the amplitude at the LFS midplane, and the HFS response also changes with $\Delta\phi$.

It is important to notice that the particular $\Delta\phi$ dependencies described in this manuscript are specific to this equilibrium, as it is in general sensitive to quantities like q_{95} and β_N [39].

3.2. Singular value decomposition (SVD) calculations

To better understand the different dependencies of the plasma response on $\Delta\phi$, SVD [40] is used, similarly to what was presented in [41]. The SVD is a matrix factorization technique commonly used in linear algebra and data analysis. SVD breaks down a matrix into three separate matrices, which represent the original matrix's essential components. Mathematically, for an $m \times n$ matrix A, the SVD factorizes it into the product of three matrices: U, W, and V:

$$A = UWV^T \tag{7}$$

where:

- U is an $m \times m$ orthogonal matrix. Its columns are known as the left singular vectors of A and provide information about the relationships between the rows of A.
- W is an $m \times n$ diagonal matrix (with possible zero entries) that contains the singular values of A in descending order

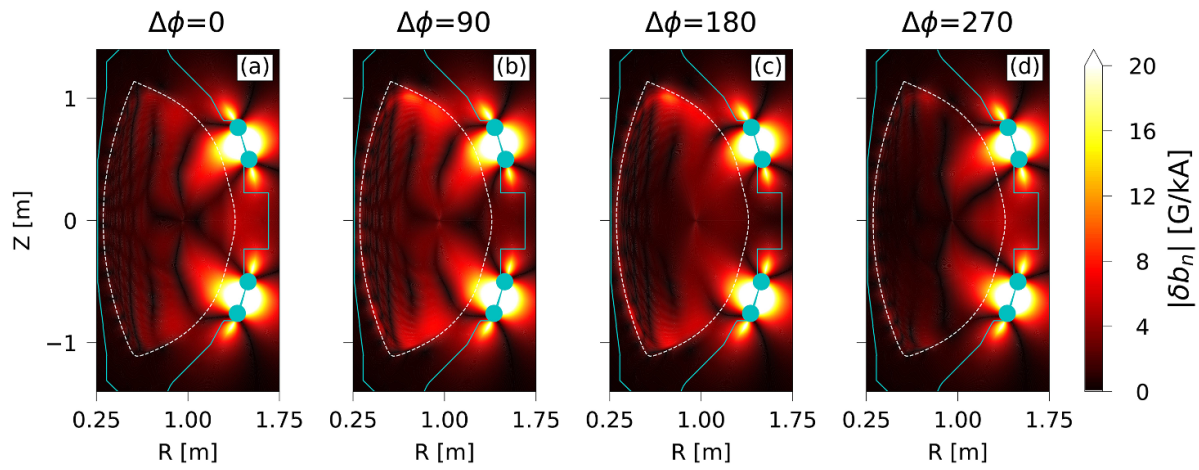

Figure 3. Predicted perturbed magnetic field perpendicular to the flux surfaces for 4 different applied $\Delta\phi$. (a) $\Delta\phi = 0°$, (b) $\Delta\phi = 90°$, (c) $\Delta\phi = 180°$, (d) $\Delta\phi = 270°$.

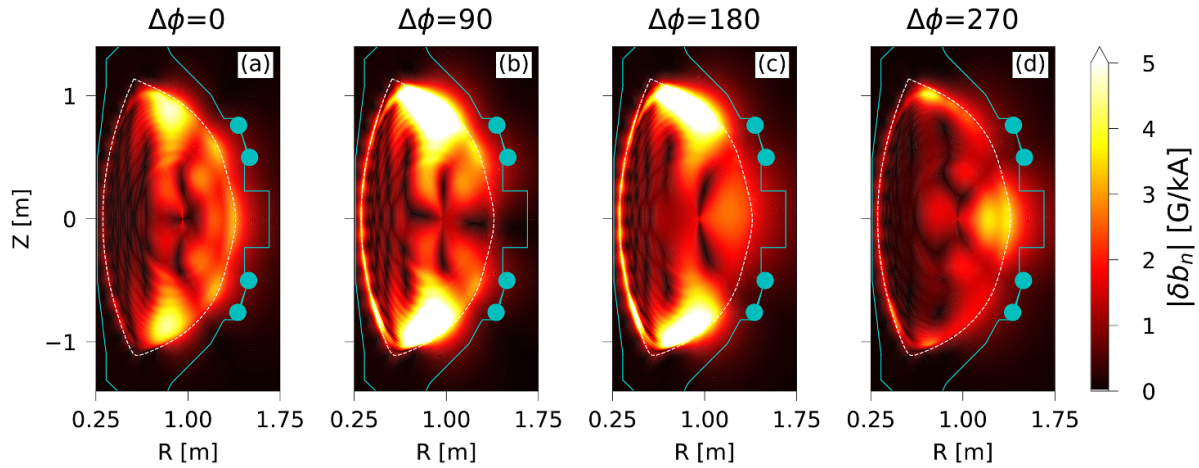

Figure 4. Predicted plasma contribution to the perturbed magnetic field perpendicular to the flux surfaces for 4 different applied $\Delta\phi$. (a) $\Delta\phi = 0°$, (b) $\Delta\phi = 90°$, (c) $\Delta\phi = 180°$, (d) $\Delta\phi = 270°$.

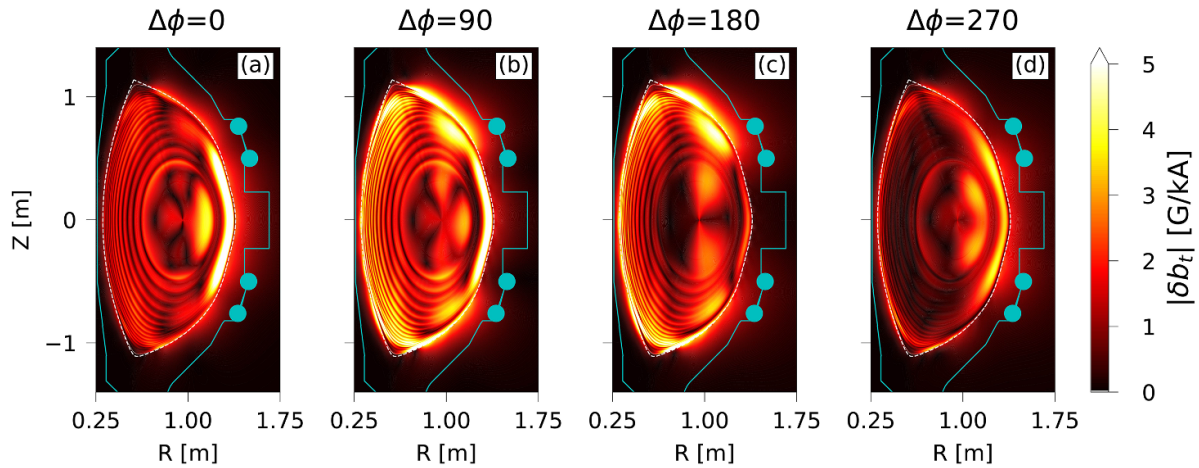

Figure 5. Predicted plasma contribution to the perturbed magnetic field tangent to the flux surfaces for 4 different applied $\Delta\phi$. (a) $\Delta\phi = 0°$, (b) $\Delta\phi = 90°$, (c) $\Delta\phi = 180°$, (d) $\Delta\phi = 270°$.

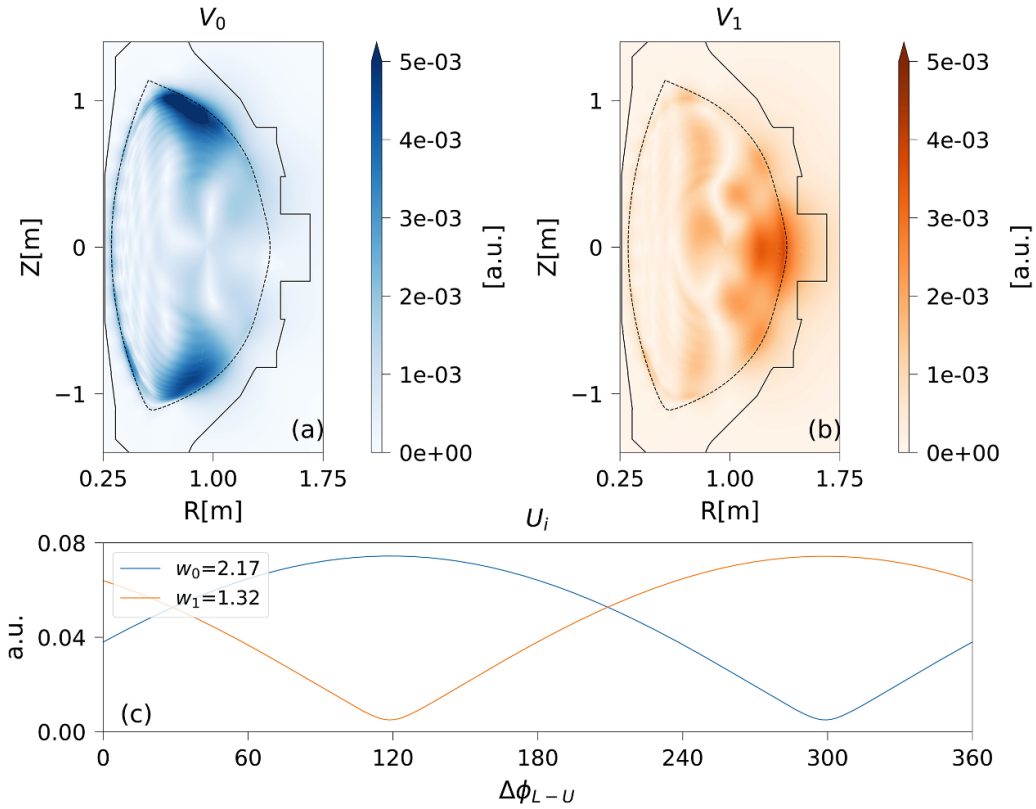

Figure 6. Poloidal structure (right singular vectors) of the dominant (a) and secondary (b) modes and their dependence on $\Delta\phi$ (left singular vectors) (c) as calculated by the Singular Value Decomposition of the predicted plasma contribution to the perturbed magnetic field perpendicular to the flux surfaces. The singular value of each of the two modes is reported in the legend of panel (c).

on the diagonal. Singular values represent the importance or 'strength' of each dimension of the data.

- V^T is the transpose of an $n \times n$ orthogonal matrix V. Its columns are known as the right singular vectors of A and provide information about the relationships between the columns of A.

Figure 6 shows the results of the application of SVD to the MARS-F simulations of figure 4. The rows of the matrix A contain the dependence of δb_n on $\Delta\phi$, while each column corresponds to a grid element. V_0 and V_1—the right singular vectors of A—are the two modes that compose the plasma response, with V_0 the mode with a larger singular value. U_0 and U_1—the left singular vectors of A—are their dependence on $\Delta\phi$.

As already suggested by the plots in figure 4, the two modes are characterized by one with a response focused on the top and bottom of the plasma, while the other has a response focused on the LFS midplane. The dominant mode has an energy almost double that of the secondary mode, and the 2 modes have a complementary dependence on $\Delta\phi$, with the dominant mode peaking around $\Delta\phi = 120°$ and having a minimum at $\Delta\phi = 300°$, and the secondary mode peaking around $\Delta\phi = 300°$ and having a minimum at $\Delta\phi = 120°$.

A similar result is also obtained for the tangential component of the magnetic field, as it is possible to see in figure 7. Also in this case the dominant mode is focused on the top and bottom of the machine and on the HFS, while the secondary mode is focused on the LFS midplane. Their dependence on $\Delta\phi$ is slightly shifted toward larger values with respect to the δb_n case. The apparent discrepancy in the energy of the dominant mode can be explained by a different amplitude of V_0, such that the product of the two does not change in the δb_n and the δb_t cases.

If the SVD is applied to the total field (vacuum plus plasma response), the results are similar, with the dependence of the modes on $\Delta\phi$ shifted by about 60° toward lower values. This can be seen in figure 8.

Although the modes extracted by the SVD do not provide direct information on the physical mode structure, the plasma response calculated by MARS-F at $\Delta\phi = 60°$ will provide information about the dominant mode since the secondary mode vanishes at such relative phase, while the opposite will be true at $\Delta\phi = 240°$. The spectrograms of the vacuum and of total field in response to the applied perturbation for these two cases are shown in figure 9. The dashed black line represent the resonant components ($m = nq$), with the crosses identifying the rational surfaces.

It is possible to see that although both phases show a screening of the field for $m \leqslant nq$, only for $\Delta\phi = 60°$ is an amplification of $m > nq$ present at the edge—the so called 'kink-peeling' response, responsible for ELM mitigation [24]—making this the most favorable RMP coil configuration to

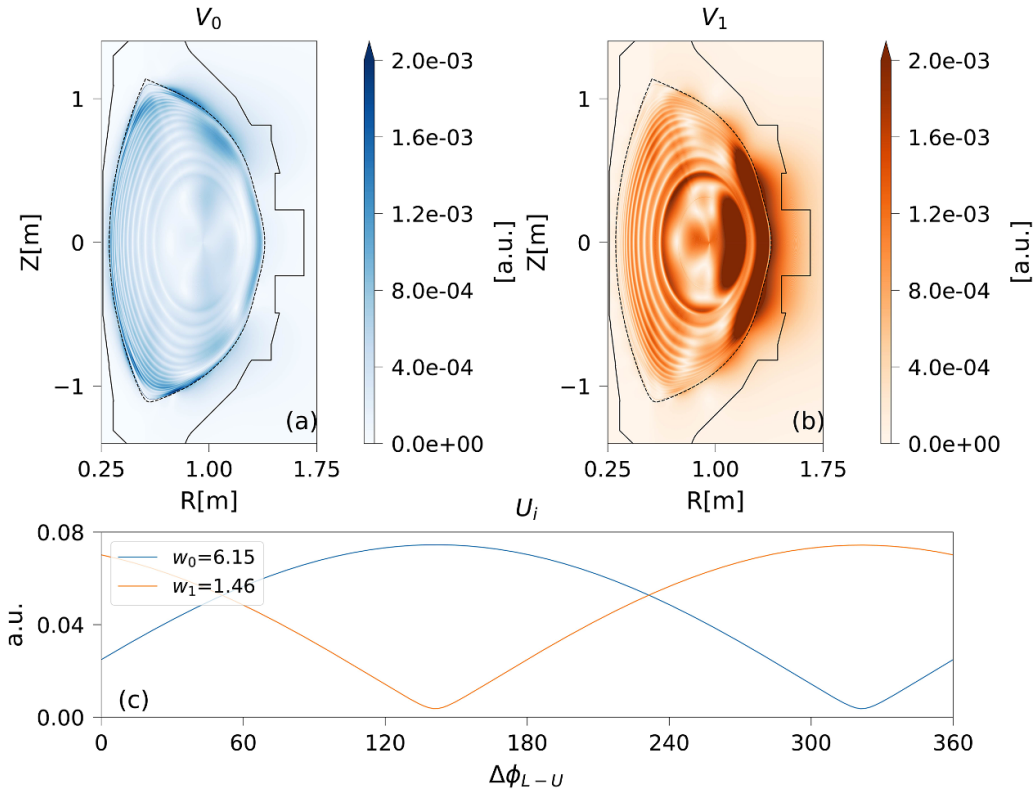

Figure 7. Poloidal structure (right singular vectors) of the dominant (a) and secondary (b) modes and their dependence on $\Delta\phi$ (left singular vectors) (c) as calculated by the Singular Value Decomposition of the predicted plasma contribution to the perturbed magnetic field tangent to the flux surfaces. The singular value of each of the two modes is reported in the legend of panel (c).

observe it for this equilibrium. This is shown in more detail in figure 10, where in panel (a) the amplitude of the $m = nq$ component is shown and in panel (b) that of the $m = nq + 3$. For both phases the resonant component of the field is strongly reduced, except at the edge where there is a higher resistivity. On the contrary, in the non-resonant case an overall amplification of the field is evident for $\Delta\phi = 60°$, that is larger close to the edge, while a screening of the field at the edge and an amplification toward the core is observed for $\Delta\phi = 240°$. Such behavior is consistent with previous DIII-D studies [41] where the core/LFS mode was also found to be correlated with a core-kink mode.

It is important to notice that the original matrix to be decomposed A is created by rows that are each a linear combination of the calculated plasma response to the upper and to the lower row of coils. This means that the original matrix is the combination of two linearly independent vectors. As a consequence it is expected that the SVD of the A matrix provides only two non-zero singular values, that correspond to the only two independent modes shown. Moreover, the SVD applied to the vacuum field results in the combination of the even and odd parity cases, also as expected.

4. Impact on measurable quantities

Since a direct measurement of the poloidal structure of the magnetic field is challenging, in this section the same analysis is performed on quantities that could be measured on MAST-U, in order to identify a method that could be used as a proxy to measure the peeling plasma response. In particular three quantities are considered: the magnetic field at the wall, the plasma displacement, and the 3D footprints at the divertor plates.

4.1. Magnetic field at the wall

Figure 11 shows the real component of the magnetic field perpendicular to the wall for $\Delta\phi = 120°$ and $\Delta\phi = 300°$ due to the plasma response, as it would be measured by 10 000 1 mm long sensors equally spaced along the wall. The horizontal axis corresponds to the toroidal angle and the vertical axis to the distance along the wall from the HFS midplane in the clockwise direction (s). It is possible to notice that at $\Delta\phi = 120°$ a larger HFS response is expected compared to $\Delta\phi = 300°$, as well as a more broad LFS one.

Figure 12 shows the result of the SVD applied to predicted measurement of the magnetic field perpendicular to the wall. This figure shows that it is possible to identify at the wall the presence of two modes, with a dominant one larger at the HFS and off-midplane in the LFS and a secondary one that is peaked at the LFS midplane. At the same time, their dependence on $\Delta\phi$ is sligtly different, with the dominant mode peaking at about $\Delta\phi \simeq 150°$, about 30° more than the optimal relative phase.

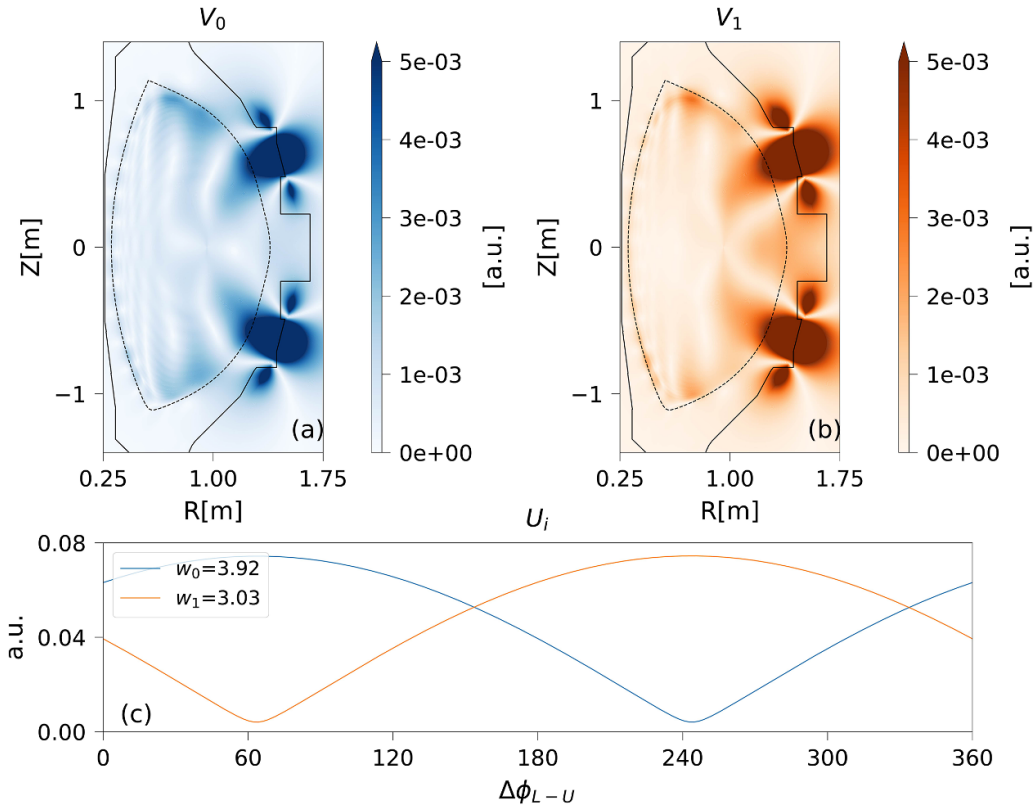

Figure 8. Poloidal structure (right singular vectors) of the dominant (a) and secondary (b) modes and their dependence on $\Delta\phi$ (left singular vectors) (c) as calculated by the Singular Value Decomposition of the predicted perturbed magnetic field perpendicular to the flux surfaces. The singular value of each of the two modes is reported in the legend of panel (c).

This difference is due to the distance of the wall from the LCFS. This can be seen in figure 13, where the SVD is calculated at three different computational surfaces located outside the separatrix. While the magnetic field normal to the closest surface to the LCFS has a similar decomposition to that of figure 6, as shown in the subplots (b) and (c) of figure 13, the poloidal structure of the two modes becomes less distinguishable moving farther away, see for example the HFS response in panels (b), (d) and (f). As a consequence their dependence on $\Delta\phi$ also changes, both in terms of minimum and maximum locations and sharpness.

In MAST-U there are six toroidal arrays of saddle coils [35], two in the HFS, one above and one below the midplane (called CSA and CSB respectively), two overlapping but of different size in the LFS midplane (called OML and OMS where the trailing character stands for large and small respectively), one in the LFS above the midplane called USL, and one in the LFS below the midplane called LSL. They are shown in magenta on figure 3. In figure 14 the SVD applied to their predicted measurement is reported. Such a set of arrays is predicted to be sufficient to reproduce the predicted poloidal shape of the plasma response at the wall.

4.2. Plasma displacement

The plasma displacement is another quantity that could be measured. Figure 15 shows the amplitude of the perpendicular displacement (ξ_n) of the LCFS as function of the coils' relative phase and the poloidal angle. It is evident that the dependence of the displacement on $\Delta\phi$ at the top and bottom of the machine is different from that at the LFS midplane.

This is highlighted also from the SVD applied to ξ_n. The results are shown in figure 16. Panels (a) and (b) are the poloidal cross section of the Real and Imaginary part of the two modes. Panel (c) shows their amplitude as function of the poloidal angle (in equal-arc coordinate) and panel (d) their dependence on $\Delta\phi$. As suggested by figure 15 the dominant mode is peaked off midplane and reaches the largest displacement for $\Delta\phi \simeq 120°$, while the amplitude of the secondary mode is larger on the LFS midplane.

It is important to notice that the dependence of the two modes on $\Delta\phi$ matches that of the plasma response (see figure 6), making it a good quantity to measure the dependence of the plasma response on the coils' relative phase.

4.3. 3D footprints

It was shown in previous work [42] that also the geometry of the heat and particle fluxes at the divertor plates depends on the poloidal spectrum of the applied RMP. In this section the field line tracing capabilities that have been recently incorporated in the MARS-F code [32, 34] are used to explore the possibility of using the 3D footprints at the divertor plates [43–46]

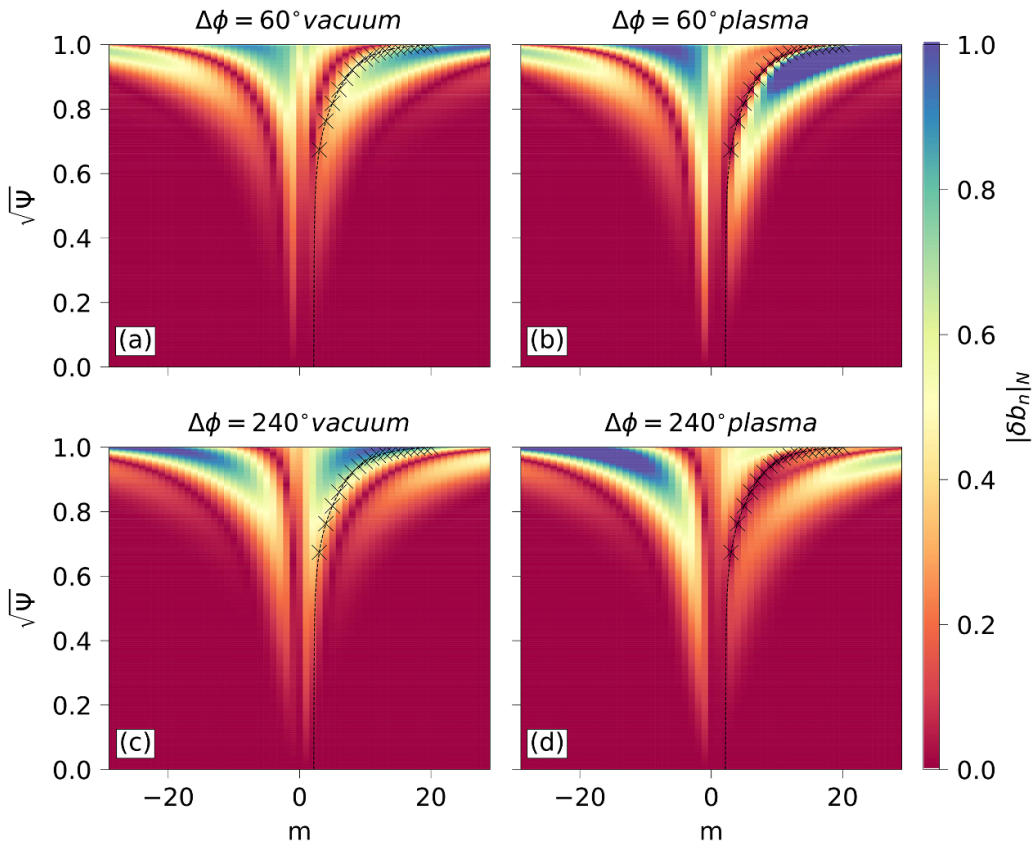

Figure 9. The poloidal spectrum of the applied perturbation neglecting (a), (c) and including (b), (d) the plasma response for $\Delta\phi = 60°$ (a), (b) and for $\Delta\phi = 240°$ (c), (d). The pitch aligned components are highlighted by black crosses, and the black dashed lines follow the $m = nq(\sqrt{\Psi})$ contour. The color scale is normalized by the maximum value in panel (a).

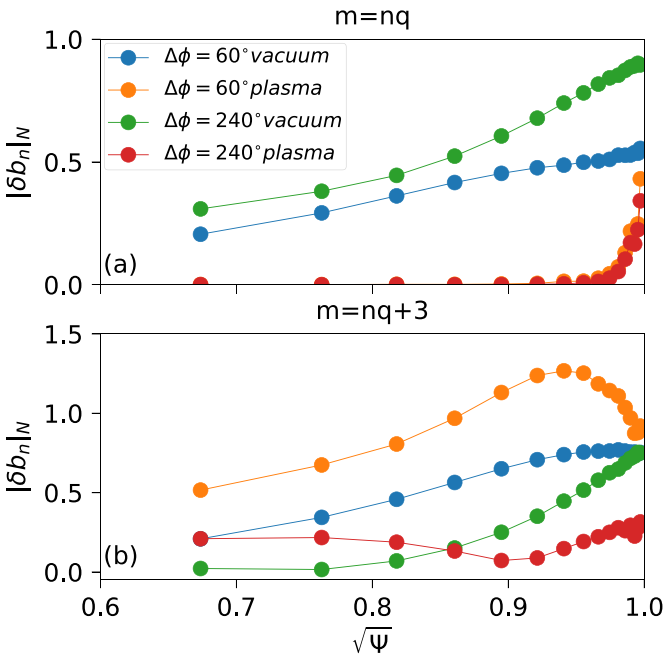

Figure 10. Pitch aligned components (a) and non resonant components (b) of the applied vacuum perturbation (in blue and green) and of the total perturbation including the plasma response (orange and red). The amplitude is normalized by the maximum value in figure 9(a).

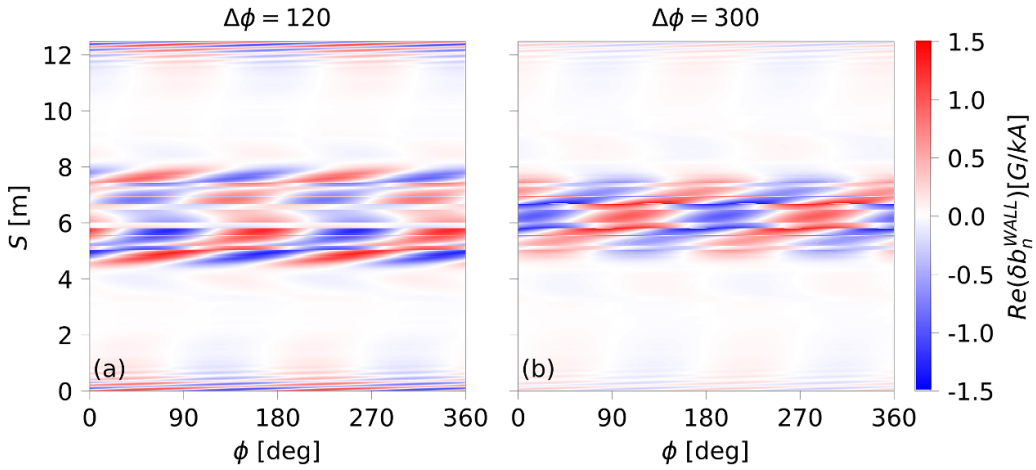

Figure 11. Real component of the perturbed magnetic field perpendicular to the MAST-U wall for $\Delta\phi = 120°$ (a) and for $\Delta\phi = 300°$ (b).

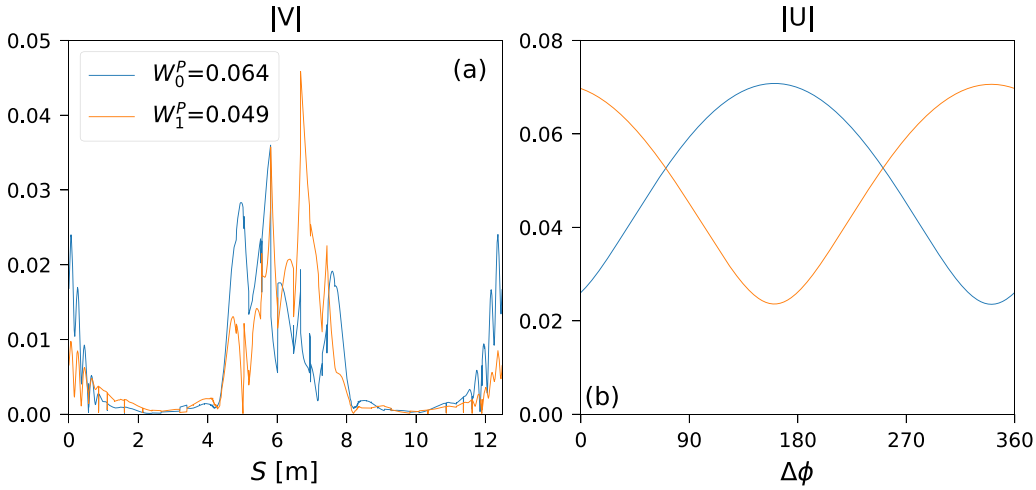

Figure 12. Poloidal structure (a) and $\Delta\phi$ dependence (b) of the 2 modes producing the predicted perturbed magnetic field perpendicular to the MAST-U wall as computed by the SVD.

to infer the plasma response dependence on $\Delta\phi$. A correlation between the magnetic footprints and the heat fluxes can be found considering a 3D version of the Eich-profile [47, 48], that shows how the field line penetration depth (which corresponds to one minus the minimum unperturbed ψ_N that perturbed open fields can reach) plays a crucial role in determining the heat fluxes to the plasma facing components. In this section the impact of the applied perturbation on both the size of the magnetic footprints and the penetration depth will be presented.

In figure 17, on the top two Poincaré plots showing island overlapping and on the bottom the correspondent magnetic footprints in the upper outer divertor are shown for two different applied $\Delta\phi$, 90° on the left and 270° on the right. The plots in (b) and (c) are made following 200 equally spaced field lines launched both toward positive and negative toroidal angles from the LFS midplane, with $0.98 \leqslant \sqrt{\psi_N} \leqslant 1$. The colors correspond to the initial $\sqrt{\psi_N}$, the abscissa to the poloidal angle in the equal-arc coordinate system used by MARS-F and the ordinate to $\sqrt{\psi_N}$. The plot in (a) corresponds to the plot in (b) mapped on a poloidal cross section, with the solid black line showing the limiter in MAST-U. The plots in (d) and (e) are made following field lines launched by a grid with 360 points in the toroidal direction (abscissa) and 200 points from $s = 1.945$ m to $s = 1.96$ m, with s the distance from the HFS midplane along the wall, in the clockwise direction (ordinate). The colors correspond to the minimum unperturbed ψ_N reached by the field line, with in white the field lines that have always $\psi_N > 1$. The amplitude of the applied perturbation is set to $I_{\mathrm{RMP}} = 1$ kA. These parameters are used for all the simulations in this section, except when otherwise specified.

The presence of island overlapping allows field lines that would have been otherwise confined within the LCFS to cross the unperturbed separatrix ($\psi_N = 1$) and become open field lines. For $\Delta\phi = 90°$ a larger stochasticity is observed with respect to $\Delta\phi = 270°$. This corresponds to field lines that can reach the divertor plates from $\sqrt{\psi_N} \simeq 0.98$ when $\Delta\phi = 90°$, while for $\Delta\phi = 270°$ the minimum $\sqrt{\psi_N} \gtrsim 0.99$. Likewise for $\Delta\phi = 90°$ the extent (Δs) of the magnetic footprint is of about 10 mm, while for $\Delta\phi = 270°$ it is reduced to about 7 mm, with

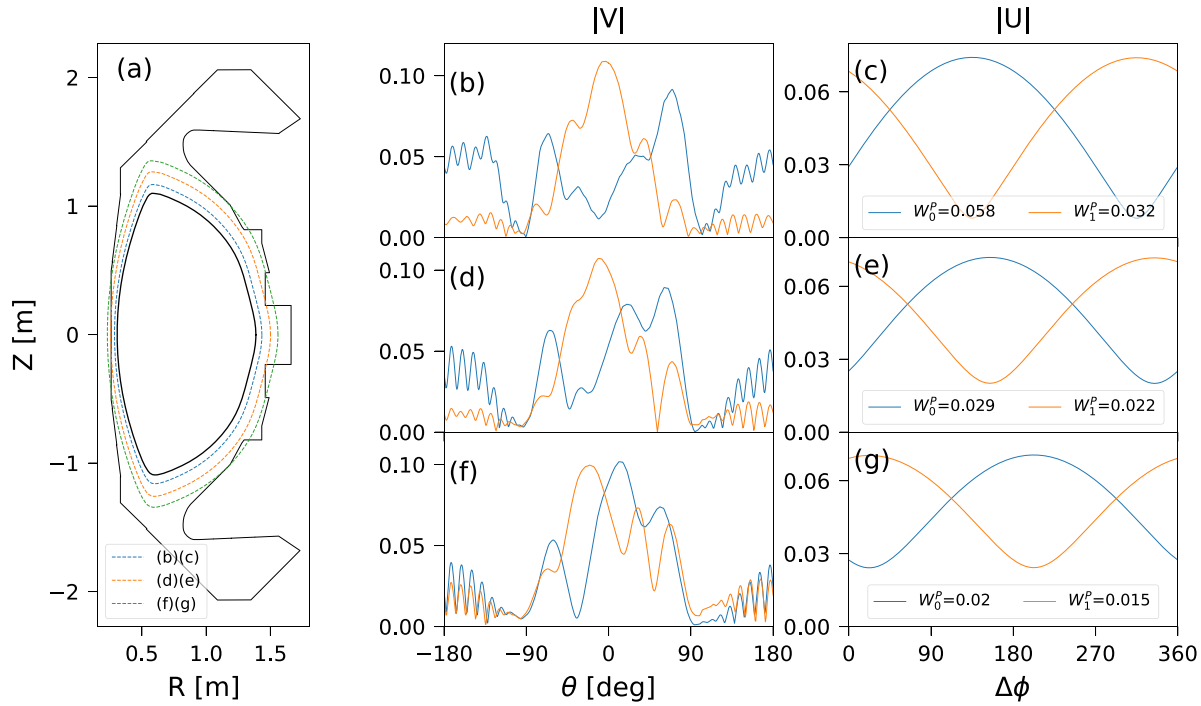

Figure 13. Poloidal structure (b), (d), (f) and $\Delta\phi$ dependence (c), (e), (g) of the 2 modes producing the predicted perturbed magnetic field perpendicular to computational surfaces shown by the dashed lines in (a) as computed by the SVD. (b) and (c) correspond to the innermost computational surface, while (f) and (g) to the outermost one. In black in (a) the LCFS and the limiter are also shown.

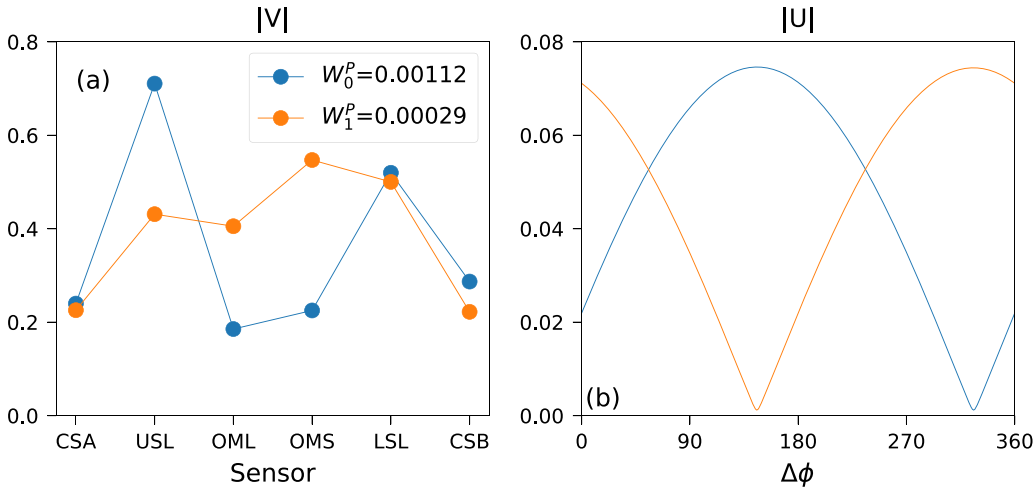

Figure 14. Poloidal structure (a) and $\Delta\phi$ dependence (b) of the 2 modes producing the predicted perturbed magnetic field measured by the 6 toroidal arrays of saddle loops as computed by the SVD.

Δs defined as the difference between the largest and the smallest value of s for which the minimum $\psi_N < 1$. Figure 17(a) moreover shows that such perturbation allows field lines from within the unperturbed separatrix to reach the divertor plate not only close to the main outer strike point, the outer upper (OU) one in this case, but also the outer lower (OL) and the inner upper (IU) ones.

A more complete scan of $\Delta\phi$ is shown in blue in figure 18. In (a) the dependence of the penetration depth and in (b) that of the footprint extent on $\Delta\phi$ are shown. These plots show that both the penetration depth and the Δs vary with $\Delta\phi$, but their dependence is different, with the largest footprint ($\Delta s \simeq$ 11 mm) observed at $\Delta\phi = 60°$ and the smallest one ($\Delta s \simeq 6$ mm) at $\Delta\phi = 240°$, while the largest penetration depth ($1 - \Psi_{N\min} \simeq 0.028$) is observed at $\Delta\phi = 90°$ and the smallest one ($1 - \psi_{N\min} \simeq 0.007$) at $\Delta\phi = 300°$.

Figure 18 also highls the importance of considering the plasma response in such calculations. The orange traces in both plots correspond the same scan done without considering the plasma response. It is clear that neglecting the plasma response would lead to a completely different result, with field lines penetrating much deeper in the plasma (minimum $\psi_{N\min} \simeq 0.9$) and smaller Δs variations as function of $\Delta\phi$, as well as different dependencies on $\Delta\phi$.

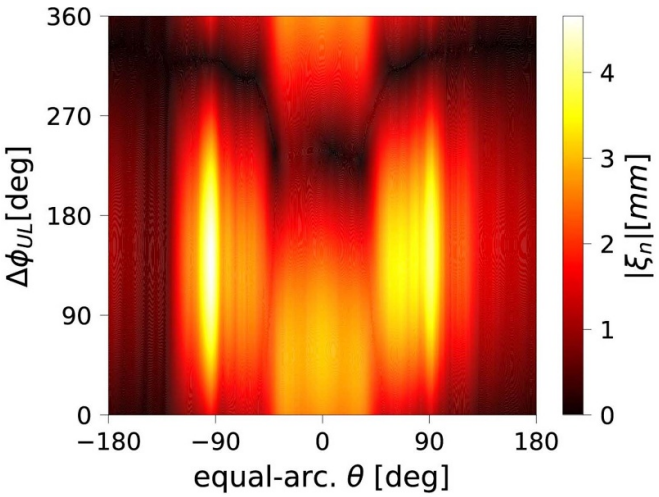

Figure 15. Predicted displacement of the LCFS as function of the poloidal angle and $\Delta\phi$.

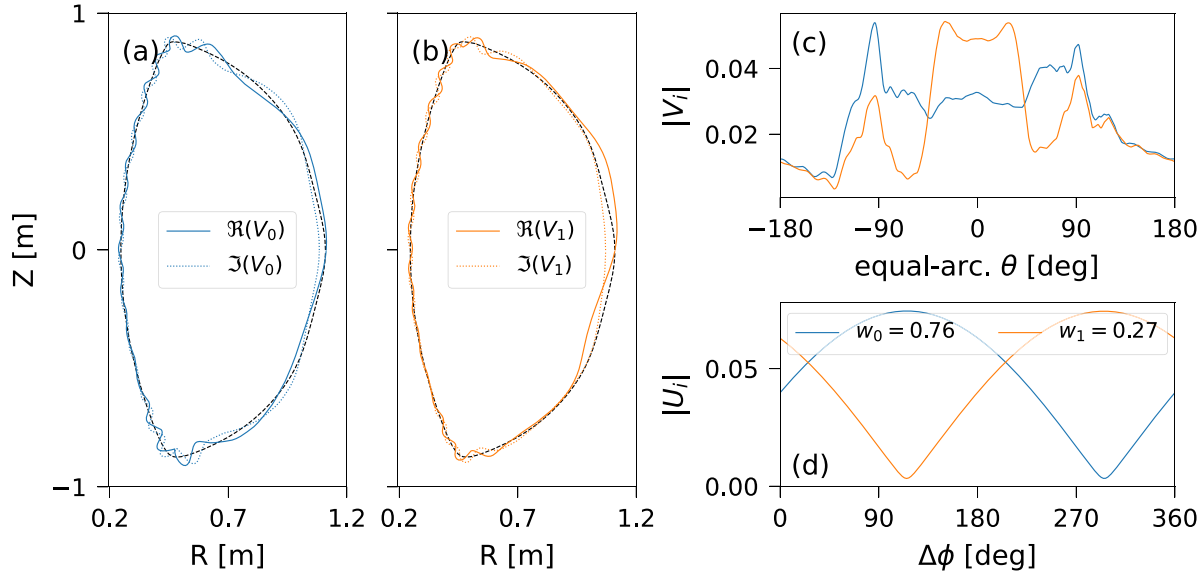

Figure 16. Real and imaginary part of the LCFS displacement poloidal structure (right singular vector) of the dominant mode (a) and of the secondary mode (b), their amplitude against the poloidal angle (c) and their $\Delta\phi$ dependence (left singular vector) (d) as computed by the SVD.

Figure 19 shows how the dependence of the penetration depth and of Δs on $\Delta\phi$ changes with the amplitude of the applied perturbation, from $I_{\mathrm{RMP}} = 0.5$ kA to $I_{\mathrm{RMP}} = 2$ kA. It is evident that a larger applied perturbation corresponds to a larger footprint that can reach deeper in the plasma. The dependence of the penetration depth and of Δs on $\Delta\phi$ is maintained, but while Δs changes almost linearly for a given $\Delta\phi$, the penetration depth has a larger change between $I_{\mathrm{RMP}} = 1$ kA and $I_{\mathrm{RMP}} = 1.5$ kA than between $I_{\mathrm{RMP}} = 1.5$ kA and $I_{\mathrm{RMP}} = 2$ kA. Moreover the overall variation in penetration depth is maintained to about 0.023, while the total variation in Δs increases from 4 mm for $I_{\mathrm{RMP}} = 1$ kA to 8 mm for $I_{\mathrm{RMP}} = 2$ kA.

Comparing these results with those in section 3.2 it is possible to observe that Δs varies with $\Delta\phi$ in the same way of the edge mode when the vacuum field and the plasma response are combined, while the penetration depth follows solely the plasma response edge mode dependency on $\Delta\phi$. This suggests that both the amplitude of the heat fluxes and their size could be used to estimate the amplitude of the edge plasma response, although the largest footprint might not correspond to the largest heat fluxes to the plasma facing components. It is also important to highlight that in [42] the footprints were calculated considering only field lines that could make a full poloidal turn, while here $\Psi_{N\mathrm{min}} < 1$ is used as threshold. If only the field lines that make a full poloidal turns are considered, the maximum and minimum values of Δs would be close to those of the penetration depth, but the overall Δs dependence becomes more complex at larger values of I_{RMP},

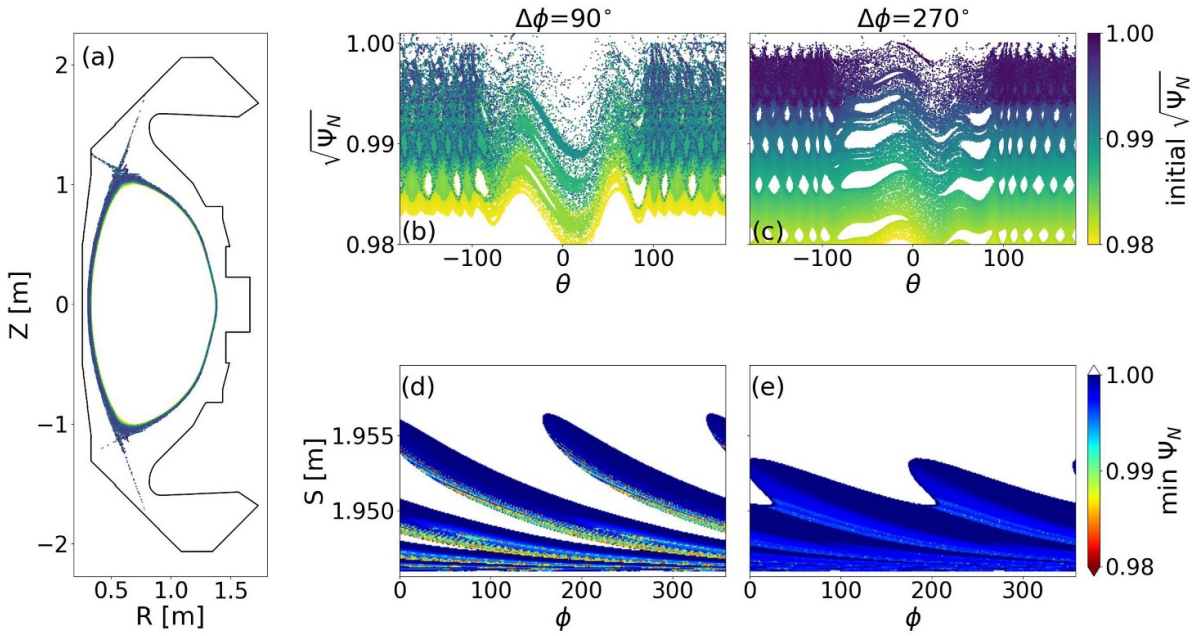

Figure 17. In (a) the poloidal cross section of MAST-U and a Poincaré plot showing the lobes extension for an applied RMP with $\Delta\phi = 90°$. In (b) and (c) the island overlapping caused by RMP with Icoil = 1kA for $\Delta\phi = 90°$ and $\Delta\phi = 270°$ respectively. In (d) and (e) the 3D footprints generated in the outer upper divertor by such perturbations.

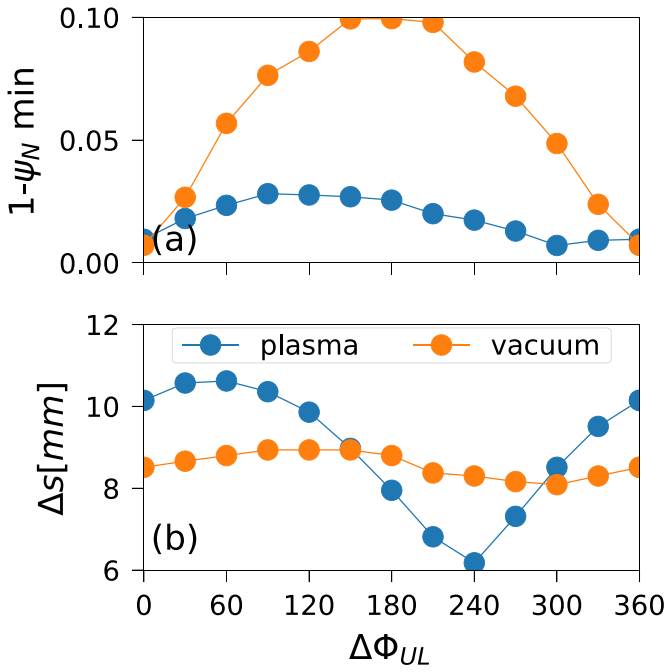

Figure 18. Dependence of the penetration depth (a) and of the magnetic footprints extent (b) in the outer upper divertor as a function of $\Delta\phi$ when the plasma response is included (blue) or neglected (orange) in the calculations.

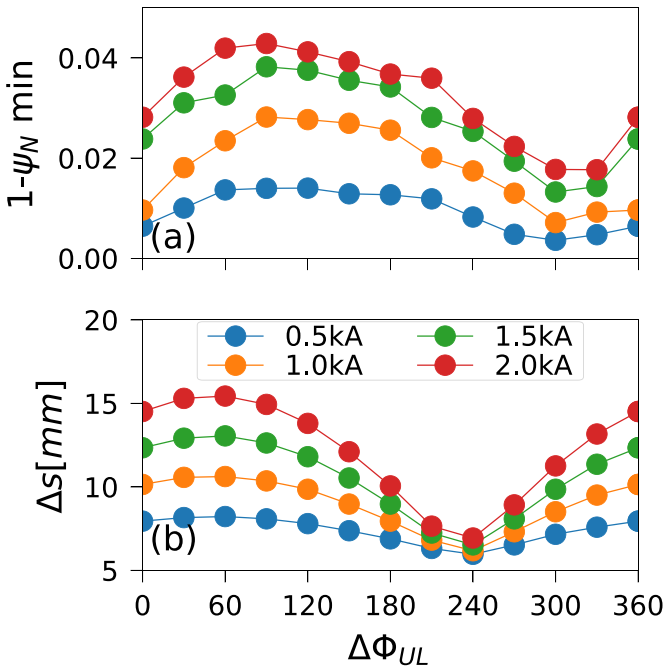

Figure 19. Dependence of the penetration depth (a) and of the magnetic footprints extent (b) in the outer upper divertor as a function of $\Delta\phi$ for different amplitudes of applied RMP.

showing a bifurcation between $\Delta\phi = 120°$ and $\Delta\phi = 180°$, as if the magnetic footprints were the intersection of two or more lobes. Although this is an interesting behaviour, it is outside the scope of this work, and it will be addressed in a future publication.

The previous two figures focused on the outer primary strike point. How the footprints change as a function of the divertor location is shown in figure 20. It is interesting to notice how the penetration depth is almost constant between the three locations chosen (except for two $\Delta\phi$), while the dependence of Δs as function of $\Delta\phi$ largely varies.

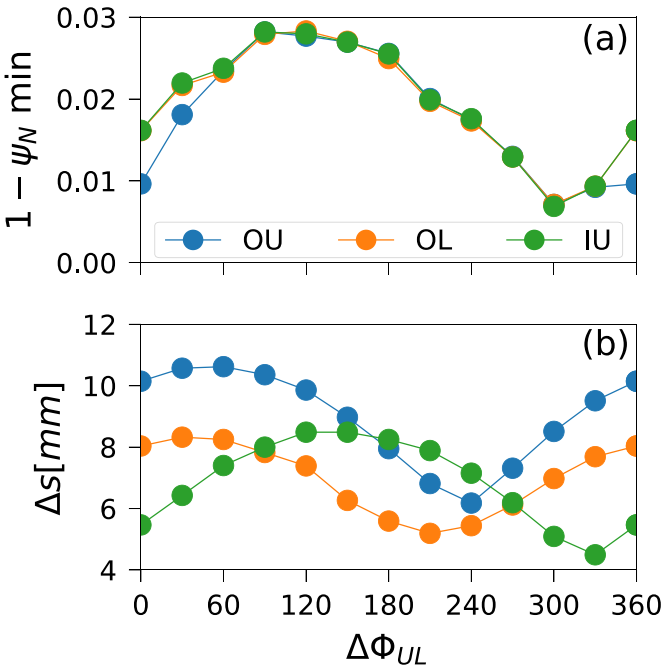

Figure 20. Dependence of the penetration depth (a) and of the magnetic footprints extent (b) as a function of $\Delta\phi$ on the different divertor plates. OU corresponds to the Outer Upper divertor, OL to the Outer Lower divertor and IU to the Inner Upper one.

5. Conclusions

In this work we studied the possibility of measuring the dependence of the perturbed magnetic field produced by the plasma in response to an applied 3D perturbation with $n = 2$ in MAST-U on the poloidal spectrum of the applied field. It was shown that poloidally distributed measurements of both the perturbed magnetic field at the wall and the displacement of the LCFS can be used to identify the two modes composing the plasma response, one poloidally localized at the LFS midplane and one above and below the midplane, and their dependence on $\Delta\phi$. In particular the displacement of the LCFS can be used as a proxy of the plasma response perpendicular to the flux surfaces. It is also shown that the poloidal position of the existing set of magnetic sensors would allow to measure the $\Delta\phi$ dependence of the 3D perturbed magnetic field at the wall, although the expected field produced by the plasma is less than 1 G/kA in most cases, making it challenging for the current magnetic diagnostic system. Last, the size of the footprints and their heat fluxes at the divertor plates are shown to have a clear dependence on the applied $\Delta\phi$, suggesting they could also be used to infer the changes in amplitude of the plasma response. Like for the magnetic field perturbations, the 3D footprints are also found to be small, with a variation in size between applied relative phases within $\Delta s = 1$ cm for $I_{\mathrm{RMP}} = 2$ kA.

The modeling results obtained provide guidance to the RMP experiments planned in MAST-U, for the purpose of measuring the multi-modal plasma response with the goal to optimize the applied poloidal spectrum in order to achieve ELM control.

Data availability statement

The data that support the findings of this study are openly available at the following URL/DOI: 10.34770/dq61-gf89 [49].

Acknowledgment

This material is based upon work supported by the US Department of Energy, Office of Science, Office of Fusion Energy Sciences, under Awards DE-AC02-09CH11466 and DE-SC0018992, and by the EPSRC Energy Programme [Grant No. EP/W006839/1].

ORCID iDs

S Munaretto https://orcid.org/0000-0003-1465-0971
Y Q Liu https://orcid.org/0000-0002-8192-8411
D A Ryan https://orcid.org/0000-0002-7735-3598
G Z Hao https://orcid.org/0000-0003-2310-6134
J W Berkery https://orcid.org/0000-0002-8062-3210
S Blackmore https://orcid.org/0000-0003-3754-6130

References

[1] Wagner F *et al* 1982 Regime of improved confinement and high beta in neutral-beam-heated divertor discharges of the ASDEX tokamak *Phys. Rev. Lett.* **49** 1408–12
[2] ASDEX Team 1989 The h-mode of ASDEX *Nucl. Fusion* **29** 1959–2040
[3] Groebner R J 1993 An emerging understanding of h-mode discharges in tokamaks *Phys. Fluids* B **5** 2343–54
[4] Leonard A W 2014 Edge-localized-modes in tokamaks *Phys. Plasmas* **21** 090501
[5] Ham C, Kirk A, Pamela S and Wilson H 2020 Filamentary plasma eruptions and their control on the route to fusion energy *Nat. Rev. Phys.* **2** 159
[6] Wilson H R, Snyder P B, Huysmans G T A and Miller R L 2002 Numerical studies of edge localized instabilities in tokamaks *Phys. Plasmas* **9** 1277–86
[7] Wilson H R, Cowley S C, Kirk A and Snyder P B 2006 Magneto-hydrodynamic stability of the h-mode transport barrier as a model for edge localized modes: an overview *Plasma Phys. Control. Fusion* **48** A71–A84
[8] Kleiner A, Ferraro N M, Canal G, Diallo A and Maingi R 2022 Critical role of current-driven instabilities for ELMs in NSTX *Nucl. Fusion* **62** 076018
[9] Loarte A *et al* (the ITPA Scrape-off Layer and Diver Group) 2007 Chapter 4: power and particle control *Nucl. Fusion* **47** S203–63
[10] Zhitlukhin A *et al* 2007 Effects of elms on iter divertor armour materials *J. Nucl. Mater.* **363–365** 301–7
[11] Loarte A *et al* 2014 Progress on the application of ELM control schemes to ITER scenarios from the non-active phase to DT operation *Nucl. Fusion* **54** 033007
[12] Burrell K H, Garofalo A M, Solomon W M, Fenstermacher M E, Osborne T H, Park J-K, Schaffer M J and Snyder P B 2012 Reactor-relevant quiescent H-mode operation using torque from non-axisymmetric, non-resonant magnetic fields *Phys. Plasmas* **19** 056117
[13] Gerhardt S P *et al* 2010 First observation of elm pacing with vertical jogs in a spherical torus *Nucl. Fusion* **50** 064015

[14] Canik J M *et al* 2010 On demand triggering of edge localized instabilities using external nonaxisymmetric magnetic perturbations in toroidal plasmas *Phys. Rev. Lett.* **104** 045001

[15] Evans T E *et al* 2004 Suppression of large edge-localized modes in high-confinement diii-d plasmas with a stochastic magnetic boundary *Phys. Rev. Lett.* **92** 235003

[16] Evans T E *et al* 2005 Suppression of large edge localized modes with edge resonant magnetic fields in high confinement DIII-D plasmas *Nucl. Fusion* **45** 595–607

[17] Evans T E *et al* 2006 The physics of edge resonant magnetic perturbations in hot tokamak plasmas *Phys. Plasmas* **13** 056121

[18] Suttrop W *et al* 2011 First observation of edge localized modes mitigation with resonant and nonresonant magnetic perturbations in ASDEX Upgrade *Phys. Rev. Lett.* **106** 225004

[19] Jeon Y M *et al* 2012 Suppression of edge localized modes in high-confinement kstar plasmas by nonaxisymmetric magnetic perturbations *Phys. Rev. Lett.* **109** 035004

[20] Kirk A *et al* 2010 Resonant magnetic perturbation experiments on mast using external and internal coils for ELM control *Nucl. Fusion* **50** 034008

[21] Kirk A, Liu Y Q, Chapman I T, Harrison J, Nardon E, Scannell R and Thornton A J 2013 Effect of resonant magnetic perturbations on ELMs in connected double null plasmas in MAST *Plasma Phys. Control. Fusion* **55** 045007

[22] Chapman I T *et al* 2014 Assessing the merits of resonant magnetic perturbations with different toroidal mode numbers for controlling edge localised modes *Nucl. Fusion* **54** 12

[23] Thornton A J, Kirk A, Cahyna P, Chapman I T, Harrison J R and Liu Y Q 2014 The effect of resonant magnetic perturbations on the divertor heat and particle fluxes in MAST *Nucl. Fusion* **54** 064011

[24] Liu Y Q, Kirk A, Gribov Y, Gryaznevich M P, Hender T C and Nardon E 2011 Modelling of plasma response to resonant magnetic perturbation fields in MAST and ITER *Nucl. Fusion* **51** 083002

[25] Paz-Soldan C *et al* 2015 Observation of a multimode plasma response and its relationship to density pumpout and edge-localized mode suppression *Phys. Rev. Lett.* **114** 105001

[26] Harrison J R *et al* (the MAST-U Team and the EUROfusion MST1 Team) 2019 Overview of new mast physics in anticipation of first results from MAST upgrade *Nucl. Fusion* **59** 112011

[27] Liu Y Q, Bondeson A, Fransson C M, Lennartson B and Breitholtz C 2000 Feedback stabilization of nonaxisymmetric resistive wall modes in tokamaks. I. Electromagnetic model *Phys. Plasmas* **7** 3681–90

[28] Liu Y Q, Kirk A and Nardon E 2010 Full toroidal plasma response to externally applied nonaxisymmetric magnetic fields *Phys. Plasmas* **17** 122502

[29] Bondeson A and Iacono R 1989 Ideal stability of cylindrical plasma in the presence of mass flow *Phys. Fluids* B **1** 1431–43

[30] Liu Y Q *et al* (EFDA JET Contributors) 2005 Feedback and rotational stabilization of resistive wall modes in ITER *Nucl. Fusion* **45** 1131–9

[31] Hao G Z *et al* 2021 Toroidal modeling of plasma response to RMP fields for Hl-2M *Nucl. Fusion* **61** 126031

[32] Liu Y Q, Parks P B, Paz-Soldan C, Kim C and Lao L L 2019 Mars-f modeling of post-disruption runaway beam loss by magnetohydrodynamic instabilities in DIII-D *Nucl. Fusion* **59** 126021

[33] Liu Y Q, Paz-Soldan C, Macusova E, Markovic T, Ficker O, Parks P B, Kim C C, Lao L L and Li L 2020 Toroidal modeling of runaway electron loss due to 3-D fields in DIII-D and COMPASS *Phys. Plasmas* **27** 102507

[34] Hao G Z *et al* 2023 Toroidal modeling of 3d perturbations generated by current filaments in scrape-off layer in tokamak with biased divertor targets *Nucl. Fusion* **63** 016006

[35] Ryan D A, Martin R, Appel L, Ayed N B, Kogan L, Kirk A and (MAST Upgrade Team) 2023 Initial progress of the magnetic diagnostics of the MAST-U tokamak *Rev. Sci. Instrum.* **94** 073501

[36] Conway N J, De Bock M F M, Michael C A, Walsh M J, Carolan P G, Hawkes N C, Rachlew E, McCone J F G, Shibaev S and Wearing G 2010 The MAST motional Stark effect diagnostica) *Rev. Sci. Instrum.* **81** 10D738

[37] Ryan D A *et al* 2015 Toroidal modelling of resonant magnetic perturbations response in ASDEX-Upgrade: coupling between field pitch aligned response and kink amplification *Plasma Phys. Control. Fusion* **57** 095008

[38] Ham C J, Cramp R G J, Gibson S, Lazerson S A, Chapman I T and Kirk A 2016 Non-axisymmetric ideal equilibrium and stability of iter plasmas with rotating RMPs *Nucl. Fusion* **56** 086005

[39] Paz-Soldan C, Logan N C, Haskey S R, Nazikian R, Strait E J, Chen X, Ferraro N M, King J D, Lyons B C and Park J-K 2016 Equilibrium drives of the low and high field side n=2 plasma response and impact on global confinement *Nucl. Fusion* **56** 056001

[40] Press W H 2007 *Numerical Recipes: The Art of Scientific Computing* (Cambridge University Press)

[41] Munaretto S, Strait E J, Haskey S R, Logan N C, Paz-Soldan C and Weisberg D B 2018 Modal analysis of the full poloidal structure of the plasma response to n=2 magnetic perturbations *Phys. Plasmas* **25** 072509

[42] Munaretto S, Orlov D M, Paz-Soldan C, Bykov I, Lasnier C J, Lyons B C and Wang H 2021 Controlling the size of non-axisymmetric magnetic footprints using resonant magnetic perturbations *Nucl. Fusion* **62** 026018

[43] Evans T E, Roeder R K W, Carter J A, Rapoport B I, Fenstermacher M E and Lasnier C J 2005 Experimental signatures of homoclinic tangles in poloidally diverted tokamaks *J. Phys.: Conf. Ser.* **7** 174

[44] Schmitz O *et al* (the TEXTOR Team) 2008 Identification and analysis of transport domains in the stochastic boundary of textor-ded for different mode spectra *Nucl. Fusion* **48** 024009

[45] Wingen A, Evans T E and Spatschek K H 2009 Footprint structures due to resonant magnetic perturbations in DIII-D *Phys. Plasmas* **16** 042504

[46] Thornton A J, Kirk A, Cahyna P, Chapman I T, Fishpool G, Harrison J R, Liu Y Q, Kripner L and Peterka M 2015 Elm mitigation via rotating resonant magnetic perturbations on MAST *J. Nucl. Mater.* **463** 723–6

[47] Eich T, Sieglin B, Scarabosio A, Fundamenski W, Goldston R J and Herrmann A 2011 Inter-elm power decay length for jet and ASDEX Upgrade: measurement and comparison with heuristic drift-based model *Phys. Rev. Lett.* **107** 215001

[48] Wingen A, Orlov D, Evans T E, Bykov I and Wilks T M 2020 New heat flux model for non-axisymmetric divertor infrared structures *Nucl. Fusion* **61** 016018

[49] Munaretto S, Liu Y Q, Ryan D A, Hao G Z, Berkery J W, Gibson S and Kogan L 2023 Data for "Chasing the multi-modal plasma response in MAST-U (https://doi.org/10.34770/dq61-gf89)